This is an open access article published under a Creative Commons Attribution (CC-BY) License, which permits unrestricted use, distribution and reproduction in any medium, provided the author and source are cited.

ACS AUTHORCHOICE

ACSNANO

www.acsnano.org

ARTICLE

Ionic Liquid Gate-Induced Modifications of Step Edges at $SrCoO_{2.5}$ Surfaces

Yuechen Zhuang,[‡] Bin Cui,[‡] Hao Yang, Fang Gao, and Stuart. S. P. Parkin*

Cite This: *ACS Nano* 2020, 14, 8562−8569

Read Online

ACCESS | Metrics & More | Article Recommendations | Supporting Information

ABSTRACT: Intense electric fields developed during gating at the interface between an ionic liquid and an oxide layer have been shown to lead to significant structural and electronic phase transitions in the entire oxide layer. An archetypical example is the reversible transformation between the brownmillerite $SrCoO_{2.5}$ and the perovskite $SrCoO_3$ engendered by ionic liquid gating. Here we show using *in situ* atomic force microscopy studies with photothermal excitation detection, that allows for high quality measurements in the viscous environment of the ionic liquid that the edges of atomically smooth terraces at the surface of $SrCoO_{2.5}$ films are significantly modified by ionic liquid gating but that the terraces themselves remain smooth. The edges develop ridges that we show, using complementary X-ray photoemission spectroscopy studies, result from the adsorption of hydroxyl groups. Our findings exhibit a way of electrically controlled surface modifications in emergent ionitronic applications.

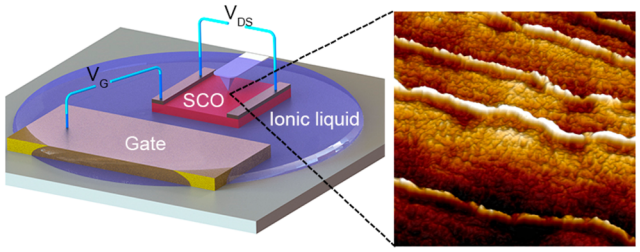

KEYWORDS: *ionic liquid gating, in situ atomic force microscopy, strontium cobaltites, hydroxyl absorption, surface structural modification*

Downloaded via MPI MICROSTRUCTURE PHYSICS on June 9, 2021 at 10:51:03 (UTC).
See https://pubs.acs.org/sharingguidelines for options on how to legitimately share published articles.

The electrical control of the crystal or electronic phase of a material is a cornerstone of many of today's electronic devices.[1] Transistor devices that use ionic liquids (ILs) allow for the development of intense electric fields within an ultrathin electric double layer (EDL) that is formed at the interface between the IL and a thin film channel.[2−5] It has been shown that these fields can lead to ion migration into and out of the film that results in structural changes or phase transformations.[6−13] These changes have potential for applications in spintronic,[14,15] sensing,[16] bio-inspired,[17] and neuromorphic[18] devices. Notably, the IL gating induced migration of ions can take place over very long distances up to microns, thus resulting in changes in physical properties of the entire bulk of a thin film.[19−21] However, the modification of the thin film surface itself has been little studied,[22,23] even though small changes in the state of the surface can strongly influence the electrochemical reactions that can take place in IL gating.[24,25] The existence of the viscous IL hinders the application of many surface sensitive characterization techniques.[26,27] There has been preliminary work investigating the ordering, dynamics, and interactions of ions in ILs at neutral and electrified solid/liquid interfaces using conventional atomic force microscopy (AFM).[28−30] Here, using photothermal excitation[31,32] we employ *in situ* AFM to investigate the evolution of the surface of $SrCoO_x$ (SCO) thin films under IL gating. We find significant changes in the morphology of the edges of atomically smooth terraces at the surfaces of these films but the terraces themselves appear unchanged. With the help of X-ray photoemission spectroscopy (XPS), we show that subnanoscale ridge structures (RSs) that emerge at the terrace edges result from reaction with hydroxyl (OH^-) groups dissolved in the ionic liquid. First-principles density functional calculations show that the terrace edges are more reactive than the terraces themselves, consistent with our experiments.

RESULTS AND DISCUSSION

IL Gate-Induced Terrace Edge Structure Modifications. In this study, 30 nm thick $SrCoO_{2.5}$ films were epitaxially grown by pulsed laser deposition on both (001) TiO_2-terminated, undoped, and 0.5 wt % Nb-doped $SrTiO_3$ substrates. The films grow in a layer-by-layer growth mode, as shown by clear oscillations in reflection high-energy electron diffraction (RHEED) intensity (see Figure S1). The topographical evolution under IL gating was *in situ* mapped within an IL droplet which covered both the $SrCoO_{2.5}$ thin film and a

Received: April 5, 2020
Accepted: July 1, 2020
Published: July 1, 2020

© 2020 American Chemical Society

https://dx.doi.org/10.1021/acsnano.0c02880
ACS Nano 2020, 14, 8562−8569

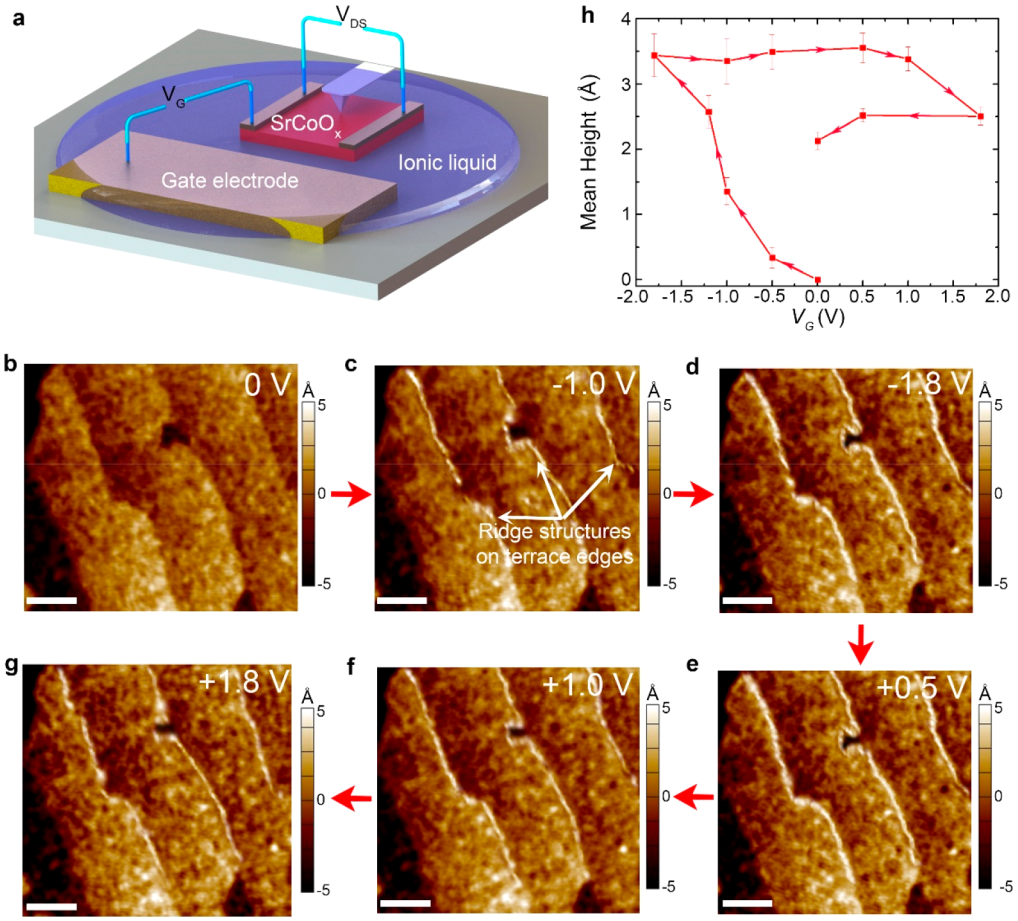

Figure 1. *In situ* AFM mapping of ridge structures under IL gating. (a) Schematic representation of the *in situ* AFM measurement combined with IL gating; *in situ* AFM topographical images at various gate voltages: (b) V_G = 0 V (pristine); (c) V_G = −1.0 V; (d)V_G = −1.8 V; (e) V_G = +0.5 V; (f) V_G = +1.0 V; (g) V_G = +1.8 V; the ridge structures are indicated by arrows in (c). All scale bars in the AFM images are 200 nm long. (h) Gate voltage-dependent mean height values of the ridge structures. The mean height is calculated from three line profiles taken from each AFM image (Figure S3) at a given V_G.

lateral Au gate electrode. The AFM cantilever was immersed in the ionic liquid EMIM-TFSI (1-ethyl-3-methylimidazolium bis(trifluoromethylsulfonyl)imide) while the surface was scanned with a gate voltage (V_G) applied, as shown in Figure 1a. We refer to EMIM-TFSI as IL in the rest of the paper. In order to clearly identify the evolution of the surface structure without damaging it, an AC (tapping) mode was used. The *in situ* AFM imaging was captured using photothermal excitation,[32] which allows for high-resolution imaging comparable to that obtained by scanning without the IL (see Figure S2 for typical images that reveal the terraces in TiO_2-terminated $SrTiO_3$ (100) in both air and IL).

Figure 1b−g illustrates typical high-resolution AFM topographical images scanned while V_G was swept as follows: 0 → −1.8 → 0 → +1.8 → 0 V. Note that V_G is applied for ∼5 min before each AFM scan at a fixed V_G. Initially, the pristine $SrCoO_{2.5}$ surface shows clear (001) terraces (Figure 1b, V_G = 0 V), consistent with a high quality epitaxial thin film (also see the RHEED results in Figure S1). The steps at the edges of the terraces are ∼4.0 Å high (Figure S3), which is consistent with the pseudotetragonal structure of $SrCoO_{2.5}$ (a_t = 3.905 Å and $c_t/4$ = 3.936 Å).[33] By applying V_G = −1.0 V for 5 min, the edges of each of the atomically flat terraces swell up, as shown in Figure 1c. The mean height of these ridged structures is h_{RS} ∼ 1.3 Å (see Supporting Information for a definition of the mean height and method used to extract it). To quantify the change in h_{RS} with V_G, we summarize the evolution of h_{RS} versus V_G in Figure 1h. As V_G is further decreased to −1.8 V, the RSs become more pronounced, as shown Figure 1d, and h_{RS} is increased to ∼3.5 Å. Subsequently, when V_G is switched to +0.5 V (Figure 1e), the RSs are maintained with an almost unchanged mean height of ∼3.5 Å, indicating that the RSs induced by IL gating are nonvolatile. Nevertheless, with further increases of V_G to +1.0 and +1.8 V, h_{RS} is reduced to ∼3.2 and ∼2.5 Å, respectively, as shown in Figure 1f,g. This confirms that the ridge structural changes are, at least in part, reversible. As distinct from the dramatic changes at the terrace edges, the flats portions of the terrace do not show any obvious response to the IL gating (the topographical profiles including RSs and terraces during a V_G cycle are shown in Figure S3). The corresponding AFM phase images indicate that the chemical compositions of the terraces and edges undergo reversible and irreversible changes, respectively, during this gating cycle (see details in Supporting Information and Figures S4 and S5).

In the following, the conductivity and crystal structure of the $SrCoO_{2.5}$ thin films are investigated under IL gating. A thin film was fabricated into a transistor device in the form of Hall-bars with lateral gate electrodes located in the vicinity of the channel. The channel is 400 μm long and 100 μm wide (ref 21). As V_G is varied from 0 to −1.8 V, the channel resistance is

https://dx.doi.org/10.1021/acsnano.0c02880
ACS Nano 2020, 14, 8562−8569

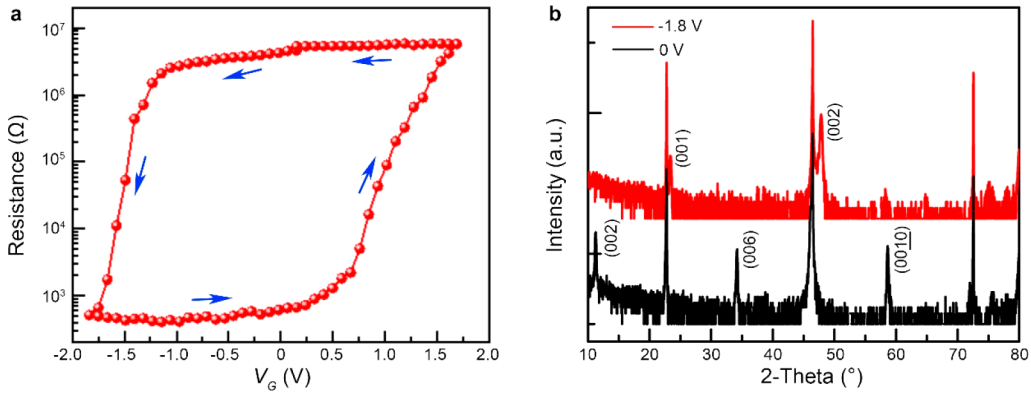

Figure 2. IL gate-induced SCO phase transition. (a) Gate voltage-dependent resistance of a 30 nm thick SCO thin film at room temperature; the resistance was measured while cycling V_G in the sequence: 0 → −1.8 → 0 → +1.8 → 0 V, as denoted by the blue arrows. Note that V_G is incremented/decremented in steps of 0.015 V: the resistance is recorded at each step (this takes ∼2 s) after V_G has been applied for 10 s (note that only every 10th data point is plotted). (b) X-ray diffraction patterns of an as-grown $SrCoO_{2.5}$ thin film (black) and the same film after IL gating at V_G = −1.8 V (red); the Miller indices of the diffraction peaks are given in the figure (these are referenced to a pseudotetragonal unit cell[33]).

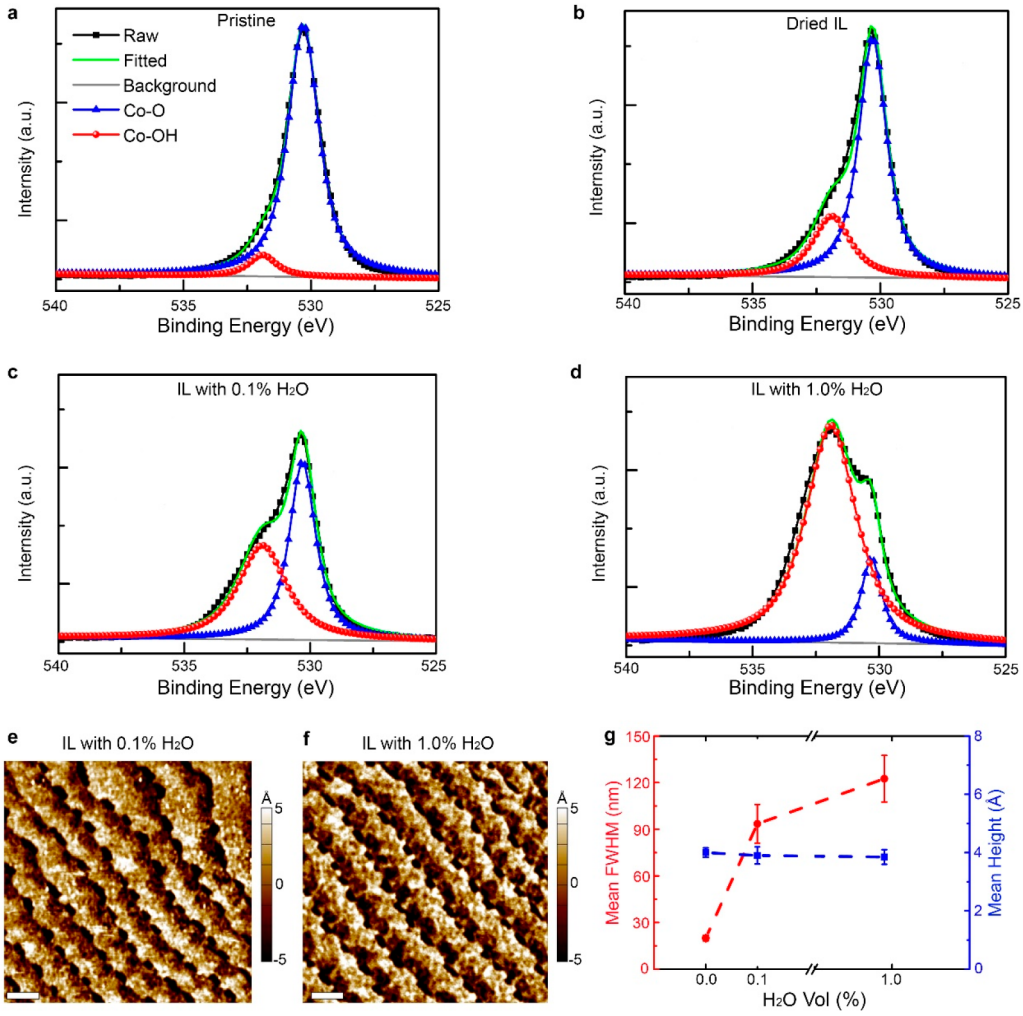

Figure 3. Effect of water on the ridge structure. XPS O-1s core-level spectra of (a) pristine $SrCoO_{2.5}$ and the same film after gating at V_G = −1.5 V using an IL without and with added H_2O; (b) dried IL; (c) IL with 0.1 vol % H_2O; (d) IL with 1.0 vol % H_2O. The XPS spectra are fitted using spectra for Co—OH (red) and Co—O[34,35] (blue). Corresponding AFM images after gating using an IL with (e) 0.1 vol % and (f) 1.0 vol % H_2O; the scale bar is 400 nm. (g) Mean fwhm (left axis) and height (right axis) of the ridge structures induced by gating with an IL without and with added H_2O of 0.1 vol % and 1.0 vol %.

reduced from 4.78×10^6 to 2.50×10^2 Ω (Figure 2a), and the initially insulating $SrCoO_{2.5}$ film becomes metallic. The resistance reverts back to 4.52×10^6 Ω when V_G = +1.8 V is applied to the sample. By cycling V_G according to 0 → −1.8 →

https://dx.doi.org/10.1021/acsnano.0c02880
ACS Nano 2020, 14, 8562−8569

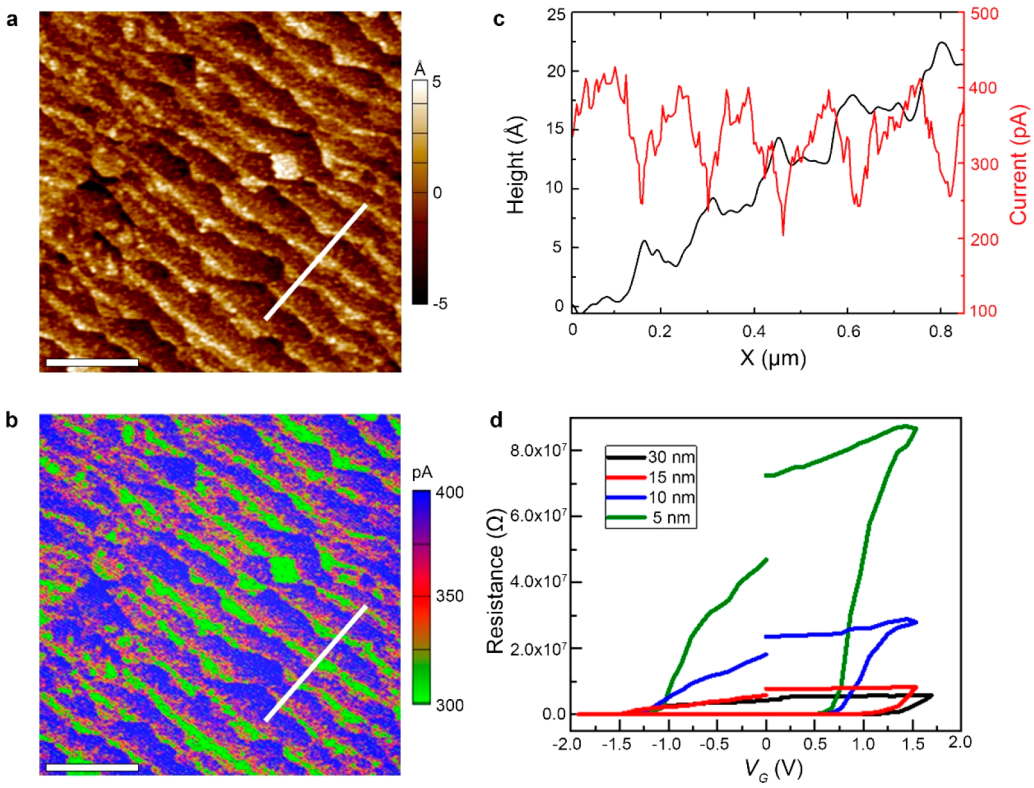

Figure 4. Electrical properties of ridge structures from cAFM and transport measurements. (a) Typical topography and (b) cAFM image for SCO thin film gated at $V_G = -1.5$V. The absolute value of the current is shown; the scale bars are 400 nm. (c) Line profiles of terraces and corresponding current extracted from (a,b) respectively. (d) V_G-dependent resistance of SCO samples with thicknesses of 5, 10, 15, and 30 nm, plotted on a linear scale.

0 → +1.8 → 0 V, the magnitude of the resistance of $SrCoO_{2.5}$ could be reversibly manipulated back and forth by nearly 4 orders of magnitude.

The X-ray diffraction (XRD) results that are shown in Figure 2b reveal that a significant structural change accompanies the IL gate-induced insulator−metal transition. The IL gating effect is nonvolatile so that the XRD could be carried out *ex situ*. The XRD of the pristine (as-grown) $SrCoO_{2.5}$ thin film clearly exhibits a characteristic quadrupled *c*-axis lattice constant expected for the brownmillerite phase which is the result of an ordered oxygen vacancy structure. Diffraction peaks corresponding to (002), (006), and (0010) of the brownmillerite phase $SrCoO_{2.5}$ can clearly be identified. A constant gate voltage $V_G = -1.8$ V was then applied for 30 min through the IL to the device. The IL was then removed by washing the device in acetone followed by isopropyl alcohol (IPA). The (002), (006), and (0010) $SrCoO_{2.5}$ diffraction peaks disappear, accompanied by shifts of the (004) and (008) diffraction peaks to higher 2-theta values. These latter two peaks correspond to the (001) and (002) peaks of the perovskite structure $SrCoO_3$, respectively. Thus, the XRD results show that IL gating at $V_G = -1.8$ V induces a structural phase transition from $SrCoO_{2.5}$ to $SrCoO_3$, which is consistent with the insulator to metal phase transition observed via the transport studies discussed above. Although the gating processes for XRD and transport measurements are different, a constant $V_G = -1.8$ V is applied for 30 min for XRD while V_G is gradually swept from 0 to −1.8 V for the transport measurements, both processes induce the full phase transition from $SrCoO_{2.5}$ to $SrCoO_3$ (Figure S6). From the XRD peak positions, we find that the out-of-plane lattice parameter (within the pseudotetragonal structure) of the initial $SrCoO_{2.5}$ layer is reduced from $c_t/4 = 3.94$ Å to $c_t = 3.80$ Å at $V_G = -1.8$ V. Scanning transmission electron microscopy (STEM) images and enlarged XRD patterns are given in Figure S7. However, such a shrinkage in the bulk lattice perpendicular to the surface of the film is not reflected in the AFM images and cannot account for the very large changes in the RSs at the terrace edges (also see Figure S8 for the STEM of ridge structure).

Interplay Between Hydroxyl and $SrCoO_x$. The phase transition between $SrCoO_{2.5}$ and $SrCoO_3$ reflected in the XRD and transport data corresponds to the bulk of the thin film. Hence, to understand the mechanism for the surface evolution during IL gating, we turn to a surface sensitive technique, namely X-ray photoelectron spectroscopy (XPS), to characterize the chemical bonding at the surface averaged over many terraces and steps (the X-ray beam is 100 μm wide). XPS was carried out on the gated samples ($V_G = -1.5$ V, the full phase transition from $SrCoO_{2.5}$ to $SrCoO_3$ is obtained as shown in Figure S6) immediately after the RSs emerge (monitored by *in situ* AFM) and after the IL was removed by ultrasonic cleaning of the sample in acetone followed by IPA. Figure 3a depicts the measured O-1s core-level spectrum and a corresponding multiple-peak fit to the data for the pristine $SrCoO_{2.5}$ sample. The fits to the XPS data use a Co—O peak that is centered at 530.3 eV and a Co—OH peak that is centered within the range 531.2 to 531.9 eV (these values are taken from refs 34 and 35). The main peak for the pristine $SrCoO_{2.5}$ is located at ∼530.4 eV, indicating that Co—O bonding is dominant. In the sample that was gated at $V_G = -1.5$ V, in addition to the main peak at ∼530.4 eV, an additional shoulder peak at the higher binding energy of ∼532.0 eV is found, which is evidence for

https://dx.doi.org/10.1021/acsnano.0c02880
ACS Nano 2020, 14, 8562−8569

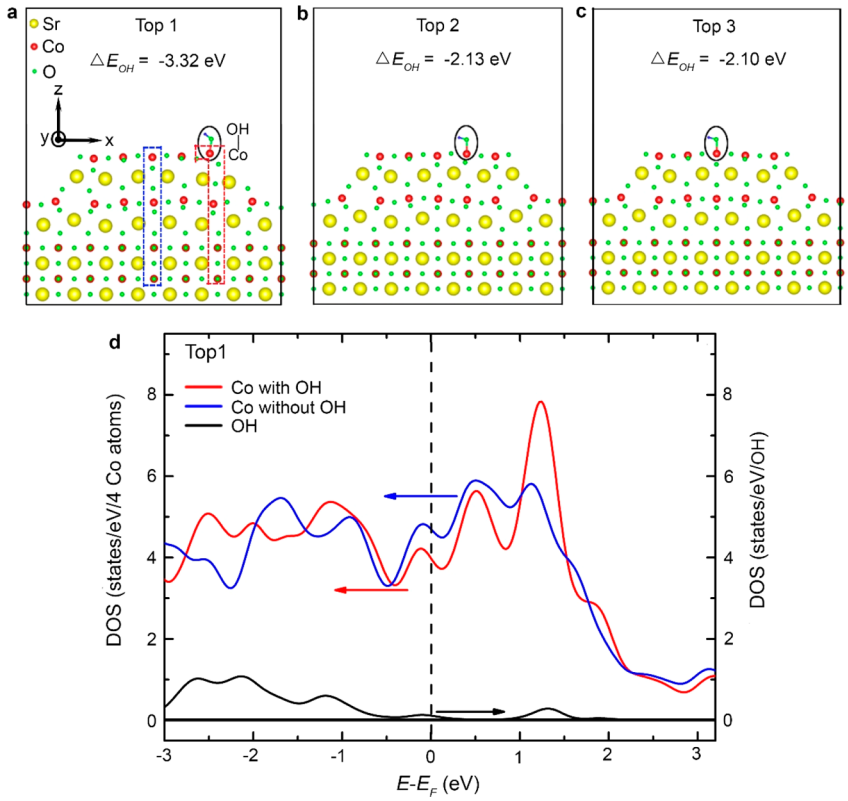

Figure 5. Calculated electronic structures of hydroxyl on a $SrCoO_3$ surface. Schematic lattices of two-dimensional slab models for $SrCoO_3$ with OH adsorbed on the terrace edge at the three unique sites (a) Top 1, (b) Top 2, and (c) Top 3. Periodic boundary conditions are applied along *x* and *y*. (d) Local DOS profiles corresponding to model Top 1, for the column of Co atoms along *z* with OH (red) at the terrace edge, and at the center of the terrace without OH (blue) and for the isolated OH (black).

the existence of Co—OH bonds (Figure 3b). The ratio, *R*, of the area within the Co—OH peak (S_{Co-OH}) to that of the sum of the areas in the Co—O and Co—OH peaks ($S_{Co-O+Co-OH}$) equals ∼0.25 in the gated sample, as compared with ∼0.07 in the pristine $SrCoO_{2.5}$ film. The origin of OH^- ions found after gating might arise from any residual H_2O dissolved in the IL. Note that for all studies, extreme care is taken to eliminate any water dissolved in the IL by drying the IL for at least half of a day in vacuum (better than 10^{-6} mbar) at 380 K. For the *in situ* AFM measurements, the IL and the sample are contained within a closed cell that is isolated from the surrounding air by a Viton O-ring seal, but some small amount of H_2O will likely be absorbed by the IL during the experiment and when the IL is exposed briefly to the air during the application of the IL onto the sample before sealing the cell. Thus, there is always some small amount of residual water in the IL even after the baking procedure mentioned above (for example, ref 12 estimates ∼0.01 vol % H_2O in EMIM-TFSI after baking).

To further confirm the role of hydroxyl groups in the formation of the RSs, we carried out gating experiments using ILs in which H_2O, in concentrations of 0.1 vol % and 1.0 vol %, was added. The Co−OH peak intensities found in the XPS studies for these two samples are dramatically enhanced with R = 0.49 (0.1 vol % H_2O) and R = 0.86 (1.0 vol % H_2O), as shown in Figure 3c,d. The AFM images of samples gated with 0.1 vol % and 1.0 vol % H_2O-IL (V_G = −1.5 V) in Figure 3e,f both show wider RSs as compared to the case for unadulterated IL (also see the profiles across the ridge structures shown in Figure S9). Figure 3g summarizes the mean height h_{RS} and fwhm (full width at half-maximum) of the RSs induced by IL gating with distinct H_2O doping levels (the mean fwhm definition and calculation methods are described in Supporting Information). After gating with V_G = −1.5 V (20 min), the h_{RS} in all three cases has a similar value of ∼4.0 Å. However, the mean fwhm of the RSs is increased from ∼20 to ∼94 nm when 0.1 vol % H_2O is added to the IL. An even greater enhancement to ∼123 nm is found for the case of 1.0 vol % H_2O. The simultaneous increase in both the mean fwhm of the RSs as well as R when using an IL with added H_2O doping supports the hypothesis that the RSs are related to an interaction between OH^- ions and the surface of SCO under negative V_G. Moreover, R = 0.21 is found after a gating procedure in which V_G is varied from 0 → −1.5 → 0 → +1.8 → 0 V, which implies that the resulting changes are only partially reversible (Figure S10).

Electrical Property of the Ridge Structures. We now turn to investigate the electrical properties of the RS and terraces. To profile the conductivity of the RSs, we utilize conductive AFM (cAFM) mapping of the leakage current through a second set of similar $SrCoO_{2.5}$ films that were prepared, however, on conducting Nb-doped $SrTiO_3$ substrates. After the sample is gated at V_G = −1.5 V for 20 min, the IL is removed by rinsing in acetone and IPA, and then cAFM is performed to map the leakage current through the terraces and the RSs. As shown in Figure 4a, one can clearly see the RSs at the terrace edges, which are almost the same as those measured in the IL (see Figure S11). Compared with homogeneous low leakage current of pristine, insulating $SrCoO_{2.5}$ (Figure S12), the corresponding leakage current image (Figure 4b) illustrates that the RSs exhibit a lower

https://dx.doi.org/10.1021/acsnano.0c02880
ACS Nano 2020, 14, 8562−8569

leakage current (green) than that of the terraces (blue). This can more readily be seen in Figure 4c where line profiles of the topography and leakage current (white solid lines in Figure 4a,b, respectively) are compared. In addition, V_G-dependent transport measurements were carried out on Hall bar devices that were patterned from samples prepared with several different thicknesses of SCO. In Figure 4d, the insulator-to-metal-to-insulator transition of a 30 nm thick sample, as V_G is varied according to 0 → −1.8 → 0 → +1.8 → 0 V, is almost fully reversible. The data shown here are the same data as those in Figure 2a but are plotted on a linear scale to magnify the resistance divergence after one V_G cycle. The resistance of a thinner 15 nm thick sample after a similar gating cycle shows a much higher resistance as compared with the initial state. Data for 10 and 5 nm thick samples are also given in Figure 4d. It is clear that as the film thickness is decreased, the contribution of the insulating RSs becomes larger, which results in larger irreversible resistance changes. It is noteworthy that cAFM measurements can clearly distinguish the current variation (∼100 pA) between RS and terraces in the direction perpendicular to the film, suggesting that the increased irreversible behavior in transport measurements is mainly due to the more insulating RSs. H_2O vol % dependent transport measurements were also performed (Figure S13); these results show more pronounced irreversible behavior as the water level was increased.

Next we carry out first-principle density functional calculations to explore the role of the hydroxyl groups in forming the RSs. We established a slab model for calculating the binding energy (ΔE_{OH}) of hydroxyl adsorbed at different sites located at various distances from a terrace edge, respectively (Top 1−3 in Figure 5a−c). Here, $SrCoO_3$ is used in the calculations since hydroxyl is absorbed at negative gating voltages at which the phase transition from $SrCoO_{2.5}$ to $SrCoO_3$ has already taken place, as demonstrated in Figure 2. As $SrCoO_{2.5}$ thin films were grown in a layer-by-layer mode on the TiO_2-terminated $SrTiO_3$ substrate (see RHEED oscillations in Figure S1), it is expected that the surface of the thin film should be CoO_2-terminated. In the slab model used in the calculations, the terrace was constructed as an 8 × 1 ($x \times y$) supercell with three $SrCoO_3$ layers in the z-direction, while the model for the terrace edge includes an additional layer in which in the x-direction is only 6 cells wide. The two lower $SrCoO_3$ layers were first fixed according to that of the calculated bulk structure and then the slab models were relaxed to obtain the ground state. Thereafter, neutral OH was added to the three positions Top 1, Top 2, and Top 3 corresponding to the three unique sites on the surface of the 6-cell wide terrace in the slab models (see Figure 5a−c). After relaxation of the final structures, the OH binding energies at these sites, ΔE_{OH}, are obtained. The calculated ΔE_{OH} (see Methods) shows that OH clearly prefers to be adsorbed at the terrace edge; the binding energy at the Top 1 site at the terrace edge is −3.32 eV while ΔE_{OH} for the interior sites on the same terrace is significantly lower (−2.13 and −2.10 eV, respectively (see Figure 5a−c)). We also calculate E_{OH} for OH^- using a similar slab model by electron doping and find that the results show the same trend as for neutral OH (see Figure S14).

The local electronic density of states (DOS) for Co and OH, located at the edge (Top 1 model), are shown in Figure 5d (neutral OH) and Figure S14d (charged OH^-). The OH is clearly insulating, meanwhile the DOS near the Fermi energy (E_F) integrated over the 4 Co atoms underneath the hydroxyl (shown by the red dashed line in Figure 5a) is lower than that of the center 4 Co atoms away from the OH (shown by the blue dashed line in Figure 5a). Therefore, the quasi-one-dimensional columnar structure formed from 4 Co atoms and the absorbed OH is less conducting, which is consistent with our experimental findings.

CONCLUSIONS

In summary, utilizing *in situ* AFM we find that IL gating of $SrCoO_x$ thin films results in significant modifications of the surface. While the morphology of the atomically flat terraces is not much changed, the edges of the terraces develop ridges that we find are due to the reaction of hydroxyl groups dissolved in the ionic liquid. These ridges are much less conducting than the terraces. Our findings imply the possibility of manipulating surfaces using ionic liquid gating when the surface has distinct morphological structures or creating nanoscale structures/interfaces with disparate conductivity, for example, with terrace edges whose spacing and orientations can be controlled by the miscut angle[36] or with hinges, formed, for example, from surface reconstructions that minimize the surface energy (*e.g.*, MgO (111) surface[37−39]). The observed terrace edge modification also shows the potential, for example, of nanostructured electrochemical interfaces in applications ranging from heterogeneous catalysis to biomedical and environmental sensing.[40,41]

METHODS

$SrCoO_{2.5}$ Thin Film Sample Preparation. $SrCoO_{2.5}$ thin films were grown on STO and Nb-STO (001) substrates at 750 °C in an oxygen pressure of 5 × 10^{-4} mbar, by pulsed laser deposition (PLD).[21] Before the deposition, all of the substrates (Crystec GmbH) were treated with buffered hydrofluoric acid [BOE 7:1 (HF:/NH_4F = 12.5%:87.5%)] for 1 min at room temperature and then annealed at 950 °C in oxygen atmosphere for 3 h to achieve TiO_2-terminated atomic terraces. The thickness of the $SrCoO_{2.5}$ films for all of the *in situ* AFM, cAFM, STEM, and XPS measurements was ∼30 nm while $SrCoO_{2.5}$ samples with thicknesses of 5, 10, and 15 nm were used for the transport measurements. After deposition, the $SrCoO_{2.5}$ films were cooled down to room temperature in the same oxygen pressure as that used for the growth.

***In Situ* AFM Characterization of IL Gating-Induced Ridge Structures.** The *in situ* AFM measurements were carried out in a Cypher (Asylum Research) atomic force microscope. An integrated blueDrive (Asylum Research) laser was used to actuate the oscillation of the cantilever (AC-55 TS, Olympus) in the IL. During AFM scanning, the cantilever, gate electrode plate (Au), and SCO sample were all covered by the IL (Figure 1a), and the gate voltage was applied by an external source meter (Keithley 2400). The ionic liquid 1-ethyl-3-methylimidazolium bis(trifluoromethylsulfonyl)imide (EMIM-TFSI), was used for all IL gating experiments. The IL and the devices were separately baked at 380 K in high vacuum (10^{-7} mbar) for at least 12 h before the gating experiments were carried out. Except for the H_2O-vol % dependent XPS measurements, dried IL was otherwise used for all measurements.

X-ray Photoelectron Spectroscopy. The X-ray photoelectron spectroscopy measurements were carried out in a Thermo Fischer Scientific K-Alpha fitted with MAGCIS and a dual mode argon ion source. Before the measurements, the gated samples were rinsed by IPA, and then immediately transferred to the XPS chamber. To remove the residual IL and other contaminants, the surface was gently treated by argon cluster ions (∼80 molecules of Argon) that do not penetrate the oxide surface and allow chemical state information to be preserved after such a cleaning process.[42] Al Kα radiation with the X-ray source operated at 14 kV with a spot size of 100 μm was used.

https://dx.doi.org/10.1021/acsnano.0c02880
ACS Nano 2020, 14, 8562−8569

Conductive AFM. Before the cAFM experiments, the SCO sample grown on a Nb-doped $SrTiO_3$ substrate was gated ($V_G = -1.5$ V for 20 min), and the development of the RSs was monitored by *in situ* AFM (see Figure S11). The Nb-doped $SrTiO_3$ substrate was sealed by paraffin to avoid current leakage.[21] After gating, the sample was rinsed by acetone and IPA to remove the residual IL and paraffin. In the cAFM measurements, a constant voltage of −5.0 V was applied to the sample holder (the tip is grounded) and the current flowing through the sample (perpendicular to the surface) is mapped. A 500 MΩ resistor was connected in series with the sample to prevent saturation of the amplifier during the measurements, and a low-noise trans-impedance amplifier (ORCA module, Asylum Research) was used that allowed for a current measurement as low as ∼1.5 pA. A conductive diamond probe (AD-2.8-AS, Adama Innovations) was used for cAFM, and the radius of the tip was ∼10 ± 5 nm.

Transport Measurements. The devices for transport measurements were prepared by photolithography and wet etching in the form of Hall-bars with lateral gate electrodes located in the vicinity of the channel. The channel was 400 μm long and 100 μm wide. Electrical contacts to the edges of the channel were formed from Au (60 nm)/Cr (10 nm) that was deposited by thermal evaporation.

First-Principles Calculations. All calculations were performed by a density function theory (DFT) method as implemented in the Vienna *ab initio* Simulation Package (VASP).[43] The Perdew−Burke−Ernzerhof (PBE) pseudopotentials with the generalized gradient approximation (GGA) were used in the calculations.[44] All structures contain a vacuum space larger than 17 Å between successive slabs and were relaxed until the atomic forces on the atoms are less than 0.02 eV $Å^{-1}$. Spin polarization was included in all calculations. The Co atoms were set to be ferromagnetic with a Hubbard U set to be 2.5 Ev.[45] The binding energy was calculated from

$$\Delta E_{OH} = E(\text{slab} + \text{OH}) - E(\text{slab}) - E(\text{OH})$$

where E(slab + OH), E(slab), and E(OH) are the energies of the composite system, the clean slab, and the uncoordinated adsorbate, respectively.

ASSOCIATED CONTENT

Supporting Information

The Supporting Information is available free of charge at https://pubs.acs.org/doi/10.1021/acsnano.0c02880.

> $SrCoO_{2.5}$ thin film sample preparation and RHEED patterns, mean height, and fwhm calculation of ridge structures; profiles of terraces as a function of gating voltages; surface chemical composition (phase) evolution; STEM images and XRD patterns of SCO induced by IL gating. XPS of O 1s core-level spectra of reverse gating SCO; electronic structures of charged hydroxyl on the $SrCoO_3$ surface (PDF)

AUTHOR INFORMATION

Corresponding Author

Stuart. S. P. Parkin − *Max Planck Institute for Microstructure Physics, Halle, Saale 06120, Germany;* orcid.org/0000-0003-4702-6139; Email: stuart.parkin@mpi-halle.mpg.de

Authors

Yuechen Zhuang − *Max Planck Institute for Microstructure Physics, Halle, Saale 06120, Germany*

Bin Cui − *Max Planck Institute for Microstructure Physics, Halle, Saale 06120, Germany*

Hao Yang − *Max Planck Institute for Microstructure Physics, Halle, Saale 06120, Germany*

Fang Gao − *Max Planck Institute for Microstructure Physics, Halle, Saale 06120, Germany;* orcid.org/0000-0002-1435-6804

Complete contact information is available at: https://pubs.acs.org/10.1021/acsnano.0c02880

Author Contributions

‡Y.Z. and B.C. contributed equally.

Author Contributions

S.S.P.P. conceived and supervised the work. Y.Z. conducted the *in situ* AFM measurements. B.C. grew the samples and performed the transport and XRD measurements. Y.Z., B.C., and F.G. performed the XPS measurement. cAFM was carried out by Y.Z. and B.C. First-principles calculations were performed by H.Y. and analyzed by Y.Z, B.C., and H.Y. All authors discussed the results and Y.Z, B.C., and S.S.P.P wrote the paper with contributions from H.Y. and F.G.

Notes

The authors declare no competing financial interest.

ACKNOWLEDGMENTS

We thank T. Ma for useful discussions and N. Schammelt and A. K. Srivastava for TEM sample preparation. Part of this research was supported by the DFG through SFB 762 and EU H2020 program "Phase Change Switch". Y.Z. acknowledges The International Max Planck Research School (IMPRS) for Science and Technology of Nano-Systems for support.

REFERENCES

(1) Ahn, C. H.; Bhattacharya, A.; Di Ventra, M.; Eckstein, J. N.; Frisbie, C. D.; Gershenson, M. E.; Goldman, A. M.; Inoue, I. H.; Mannhart, J.; Millis, A. J.; Morpurgo, A. F.; Natelson, D.; Triscone, J. Electrostatic Modification of Novel Materials. *Rev. Mod. Phys.* **2006**, *78*, 1185.

(2) Hwang, H. Y.; Iwasa, Y.; Kawasaki, M.; Keimer, B.; Nagaosa, N.; Tokura, Y. Emergent Phenomena at Oxide Interfaces. *Nat. Mater.* **2012**, *11*, 103−113.

(3) Fujimoto, T.; Awaga, K. Electric-Double-Layer Field-Effect Transistors with Ionic Liquids. *Phys. Chem. Chem. Phys.* **2013**, *15*, 8983−9006.

(4) Bisri, S. Z.; Shimizu, S.; Nakano, M.; Iwasa, Y. Endeavor of Iontronics: From Fundamentals to Applications of Ion-Controlled Electronics. *Adv. Mater.* **2017**, *29*, 1607054.

(5) Leighton, C. Electrolyte-Based Ionic Control of Functional Oxides. *Nat. Mater.* **2019**, *18*, 13−18.

(6) Jeong, J.; Aetukuri, N. B.; Graf, T.; Schladt, T. D.; Samant, M. G.; Parkin, S. S. P. Suppression of Metal-Insulator Transition in VO_2 by Electric Field-Induced Oxygen Vacancy Formation. *Science* **2013**, *339*, 1402−1405.

(7) Li, M.; Han, W.; Jiang, X.; Jeong, J.; Samant, M. G.; Parkin, S. S. P. Suppression of Ionic Liquid Gate-Induced Metallization of $SrTiO_3$ (001) by Oxygen. *Nano Lett.* **2013**, *13*, 4675−4678.

(8) Lin, W.; Ding, J.; Wu, S.; Li, Y.; Lourembam, J.; Shannigrahi, S.; Wang, S.; Wu, T. Electrostatic Modulation of $LaAlO_3/SrTiO_3$ Interface Transport in a Electric Double-Layer Transistor. *Adv. Mater. Interfaces* **2014**, *1*, 1300001.

(9) Jeong, J.; Aetukuri, N. B.; Passarello, D.; Conradson, S. D.; Samant, M. G.; Parkin, S. S. P. Giant Reversible, Facet-Dependent, Structural Changes in a Correlated-Electron Insulator Induced by Ionic Liquid Gating. *Proc. Natl. Acad. Sci. U. S. A.* **2015**, *112*, 1013−1018.

(10) Zeng, S.; Lü, W.; Huang, Z.; Liu, Z.; Han, K.; Gopinadhan, K.; Li, C.; Guo, R.; Zhou, W.; Ma, H. H.; Jian, L.; Venkatesan, T.; Ariando. Liquid-Gated High Mobility and Quantum Oscillation of the Two-Dimensional Electron Gas at an Oxide Interface. *ACS Nano* **2016**, *10*, 4532−4537.

(11) Shibuya, K.; Sawa, A. Modulation of Metal-Insulator Transition in VO_2 by Electrolyte Gating-Induced Protonation. *Adv. Electron. Mater.* **2016**, *2*, 1500131.

(12) Lu, N.; Zhang, P.; Zhang, Q.; Qiao, R.; He, Q.; Li, H.; Wang, Y.; Guo, J.; Zhang, D.; Duan, Z.; Li, Z.; Wang, M.; Yang, S.; Yan, M.; Arenholz, E.; Zhou, S.; Yang, W.; Gu, L.; Nan, C.; Wu, J.; et al. Electric-Field Control of Tri-State Phase Transformation with a Selective Dual-Ion Switch. *Nature* **2017**, *546*, 124−128.

(13) Sun, Y.; Kotiuga, M.; Lim, D.; Narayanan, B.; Cherukara, M.; Zhang, Z.; Dong, Y.; Kou, R.; Sun, C.; Lu, Q.; Waluyo, I.; Hunt, A.; Tanaka, H.; Hattori, A. N.; Gamage, S.; Abate, Y.; Pol, V. G.; Zhou, H.; Sankaranarayanan, S. K. R. S.; Yildiz, B.; et al. Strongly Correlated Perovskite Lithium Ion Shuttles. *Proc. Natl. Acad. Sci. U. S. A.* **2018**, *115*, 9672−9677.

(14) Wang, Y.; Zhou, X.; Song, C.; Yan, Y.; Zhou, S.; Wang, G.; Chen, C.; Zeng, F.; Pan, F. Electrical Control of the Exchange Spring in Antiferromagnetic Metals. *Adv. Mater.* **2015**, *27*, 3196−3201.

(15) Liang, L.; Chen, Q.; Lu, J.; Talsma, W.; Shan, J.; Blake, G. R.; Palstra, T. T. M.; Ye, J. Inducing Ferromagnetism and Kondo Effect in Platinum by Paramagnetic Ionic Gating. *Sci. Adv.* **2018**, *4*, No. eaar2030.

(16) Zhang, Z.; Schwanz, D.; Narayanan, B.; Kotiuga, M.; Dura, J. A.; Cherukara, M.; Zhou, H.; Freeland, J. W.; Li, J.; Sutarto, R.; He, F.; Wu, C.; Zhu, J.; Sun, Y.; Ramadoss, K.; Nonnenmann, S. S.; Yu, N.; Comin, R.; Rabe, K. M.; Sankaranarayanan, S. K. R. S.; et al. Perovskite Nickelates As Electric-Field Sensors in Salt Water. *Nature* **2018**, *553*, 68−72.

(17) Kim, Y.; Chortos, A.; Xu, W.; Liu, Y.; Oh, J. Y.; Son, D.; Kang, J.; Foudeh, A. M.; Zhu, C.; Lee, Y.; Niu, S.; Liu, J.; Pfattner, R.; Bao, Z.; Lee, T. A Bioinspired Flexible Organic Artificial Afferent Nerve. *Science* **2018**, *360*, 998.

(18) Zhu, X.; Li, D.; Liang, X.; Lu, W. D. Ionic Modulation and Ionic Coupling Effects in MoS_2 Devices for Neuromorphic Computing. *Nat. Mater.* **2019**, *18*, 141−148.

(19) Altendorf, S. G.; Jeong, J.; Passarello, D.; Aetukuri, N. B.; Samant, M. G.; Parkin, S. S. P. Facet-Independent Electric-Field-Induced Volume Metallization of Tungsten Trioxide Films. *Adv. Mater.* **2016**, *28*, 5284−5292.

(20) Passarello, D.; Altendorf, S. G.; Jeong, J.; Rettner, C.; Arellano, N.; Topuria, T.; Samant, M. G.; Parkin, S. S. P. Evidence for Ionic Liquid Gate-Induced Metallization of Vanadium Dioxide Bars Over Micron Length Scales. *Nano Lett.* **2017**, *17*, 2796−2801.

(21) Cui, B.; Werner, P.; Ma, T.; Zhong, X.; Wang, Z.; Taylor, J. M.; Zhuang, Y.; Parkin, S. S. P. Direct Imaging of Structural Changes Induced by Ionic Liquid Gating Leading to Engineered Three-Dimensional Meso-Structures. *Nat. Commun.* **2018**, *9*, 3055.

(22) Schladt, T. D.; Graf, T.; Aetukuri, N. B.; Li, M.; Fantini, A.; Jiang, X.; Samant, M. G.; Parkin, S. S. P. Crystal-Facet-Dependent Metallization in Electrolyte-Gated Rutile TiO_2 Single Crystals. *ACS Nano* **2013**, *7*, 8074−8081.

(23) Petach, T. A.; Lee, M.; Davis, R. C.; Mehta, A.; Goldhaber-Gorder, D. Mechanism for the Large Conductance Modulation in Electrolyte-Gated Thin Gold Films. *Phys. Rev. B: Condens. Matter Mater. Phys.* **2014**, *90*, 081108.

(24) Gallagher, P.; Lee, M.; Petach, T. A.; Stanwyck, S. W.; Williams, J. R.; Watanabe, K.; Taniguchi, T.; Goldhaber-Gordon, D. A High-Mobility Electronic System at an Electrolyte-Gated Oxide Surface. *Nat. Commun.* **2015**, *6*, 6437.

(25) Yuan, H.; Shimotani, H.; Tsukazaki, A.; Ohtomo, A.; Kawasaki, M.; Iwasa, Y. Hydrogenation-Induced Surface Polarity Recognition and Proton Memory Behavior at Protic-Ionic-Liquid/Oxide Electric-Double-Layer Interfaces. *J. Am. Chem. Soc.* **2010**, *132*, 6672−6678.

(26) Zaera, F Probing Liquid/Solid Interfaces at the Molecular Level. *Chem. Rev.* **2012**, *112*, 2920−2986.

(27) Jiang, S.; Chen, Z.; Chen, X.; Nguyen, D.; Mattei, M.; Goubert, G.; Van Duyne, R. P. Investigation of Cobalt Phthalocyanine at the Solid/Liquid Interface by Electrochemical Tip-Enhanced Raman Spectroscopy. *J. Phys. Chem. C* **2019**, *123*, 9852−9859.

(28) Black, J. M.; Walters, D.; Labuda, A.; Feng, G.; Hillesheim, P. C.; Dai, S.; Cummings, P. T.; Kalinin, S. V.; Proksch, R.; Balke, N. Bias-Dependent Molecular-Level Structure of Electrical Double Layer in Ionic Liquid on Graphite. *Nano Lett.* **2013**, *13*, 5954−5960.

(29) Elbourne, A.; McDonald, S.; Voïchovsky, K.; Endres, F.; Warr, G. G.; Atkin, R. Nanostructure of the Ionic Liquid-Graphite Stern Layer. *ACS Nano* **2015**, *9*, 7608−7620.

(30) Black, J. M.; Come, J.; Bi, S.; Zhu, M.; Zhao, W.; Wong, A. T.; Noh, J. H.; Pudasaini, P. R.; Zhang, P.; Okatan, M. B.; Dai, S.; Kalinin, S. V.; Rack, P. D.; Ward, T. Z.; Feng, G.; Balke, N. Role of Electrical Double Layer Structure in Ionic Liquid Gated Devices. *ACS Appl. Mater. Interfaces* **2017**, *9*, 40949−40958.

(31) Labuda, A.; Kobayashi, K.; Miyahara, Y.; Grütter, P. Retrofitting an Atomic Force Microscope with Photothermal Excitation for a Clean Cantilever Response in Low Q Environments. *Rev. Sci. Instrum.* **2012**, *83*, 053703.

(32) Labuda, A.; Cleveland, J.; Geisse, N. A.; Kocun, M.; Ohler, B.; Proksch, R.; Viani, M. B.; Walters, D. Photothermal Excitation for Improved Cantilever Drive Performance in Tapping Mode Atomic Force Microscopy. *Microscopy and Analysis* **2014**, *28*, 21−25.

(33) Munoz, A.; de la Calle, C.; Alonso, J. A.; Botta, P. M.; Pardo, V.; Baldomir, D.; Rivas, J. Crystallographic and Magnetic Structure of $SrCoO_{2.5}$ Brownmillerite: Neutron Study Coupled with Band-Structure Calculations. *Phys. Rev. B: Condens. Matter Mater. Phys.* **2008**, *78*, 054404.

(34) Chang, J.; Wu, C.; Sun, I. Nano-Architectured $Co(OH)_2$ Electrodes Constructed Using an Easily-Manipulated Electrochemical Protocol for High-performance Energy Storage Applications. *J. Mater. Chem.* **2010**, *20*, 3729−3735.

(35) Pang, M.; Long, G.; Jiang, S.; Ji, Y.; Han, W.; Wang, B.; Liu, X.; Xi, Y.; Wang, D.; Xu, F. Ethanol-Assisted Solvothermal Synthesis of Porous Nanostructured Cobaltoxides (CoO/Co_3O_4) for High-Performance Supercapacitors. *Chem. Eng. J.* **2015**, *280*, 377−384.

(36) Viernow, J.; Lin, J.-L.; Petrovykh, D. Y.; Leibsle, F. M.; Men, F. K.; Himpsel, F. J. Regular Step Arrays on Silicon. *Appl. Phys. Lett.* **1998**, *72*, 948.

(37) Freund, H.-J.; Kuhlenbeck, H.; Staemmler, V. Oxide Surfaces. *Rep. Prog. Phys.* **1996**, *59*, 283.

(38) Goniakowski, J.; Finocchi, F.; Noguera, C. Polarity of Oxide Surfaces and Nanostructures. *Rep. Prog. Phys.* **2008**, *71*, 016501.

(39) Noguera, C. Polar Oxide Surfaces. *J. Phys.: Condens. Matter* **2000**, *12*, R367−R410.

(40) Farias, M. J. S.; Cheuquepan, W.; Camara, G. A.; Feliu, J. M. Disentangling Catalytic Activity at Terrace and Step Sites on Selectively Ru-Modified Well-Ordered Pt Surfaces Probed by CO Electro-Oxidation. *ACS Catal.* **2016**, *6*, 2997−3007.

(41) Bentley, C. L.; Kang, M.; Unwin, P. R. Nanoscale Surface Structure-Activity in Electrochemistry and Electrocatalysis. *J. Am. Chem. Soc.* **2019**, *141*, 2179−2193.

(42) Aureau, D.; Ridier, K.; Bérini, B.; Dumont, Y.; Keller, N.; Vigneron, J.; Bouttemy, M.; Etcheberry, A.; Fouchet, A. Advanced Analysis Tool for X-Ray Photoelectron Spectroscopy Profiling: Cleaning of Perovskite $SrTiO_3$ Oxide Surface Using Argon Cluster Ion Source. *Thin Solid Films* **2016**, *601*, 89−92.

(43) Kresse, G.; Furthmüller, J. Efficiency of *Ab-Initio* Total Energy Calculations for Metals and Semiconductors Using a Plane-Wave Basis Set. *Comput. Mater. Sci.* **1996**, *6*, 15−50.

(44) Perdew, J. P.; Burke, K.; Ernzerhof, M. Generalized Gradient Approximation Made Simple. *Phys. Rev. Lett.* **1996**, *77*, 3865.

(45) Lee, J. H.; Rabe, K. M. Coupled Magnetic-Ferroelectric Metal-Insulator Transition in Epitaxially Strained $SrCoO_3$ from First Principles. *Phys. Rev. Lett.* **2011**, *107*, 067601.

https://dx.doi.org/10.1021/acsnano.0c02880
ACS Nano 2020, 14, 8562−8569